Bad Neighbour, Good Neighbour: How Magnetic Dipole Interactions Between Soft and Hard Ferrimagnetic Nanoparticles Affect Macroscopic Magnetic Properties in Ferrofluids

Niéli Daffé, Jovana Zečević, Kalliopi N Trohidou, Marcin Sikora, Mauro Rovezzi, Claire Carvallo, Marianna Vasilakaki, Sophie Neveu, Johannes Meeldijk, Nadejda Bouldi, et al.

HAL Id: hal-03019997

https://hal.sorbonne-universite.fr/hal-03019997

Submitted on 23 Nov 2020

ARTICLE

Bad Neighbour, Good Neighbour: How Magnetic Dipole Interactions Between Soft and Hard Ferrimagnetic Nanoparticles Affect Macroscopic Magnetic Properties in Ferrofluids

Niéli Daffé,[a,b,c] Jovana Zečević,[d] Kalliopi N. Trohidou,[e] Marcin Sikora,[f] Mauro Rovezzi,[g] Claire Carvallo,[a] Marianna Vasilakaki,[e] Sophie Neveu,[c] Johannes Meeldijk,[d] Nadejda Bouldi,[a,b] Véronica Gavrilov,[c] Yohan Guyodo,[h] Fadi Choueikani,[b] Vincent Dupuis,[c] Dario Taverna,[a] Philippe Sainctavit,[a,b] and Amélie Juhin[a,*]

Fluids responding to magnetic fields (ferrofluids) offer a scene with no equivalent in nature to explore long-range magnetic dipole interactions. Here, we studied the very original class of binary ferrofluids, embedding soft and hard ferrimagnetic nanoparticles. We used a combination of x-ray magnetic spectroscopy measurements supported by multi-scale experimental techniques and Monte-Carlo simulations to unveil the origin of the emergent macroscopic magnetic properties of the binary mixture. We found that the association of soft and hard magnetic nanoparticles in the fluid has a considerable influence on their inherent magnetic properties. While the ferrofluid remains in a single phase, magnetic interactions at the nanoscale between both types of particles induce a modification of their respective coercive fields. By connecting the microscopic properties of binary ferrofluids containing small particles, our findings lay the groundwork for the manipulation of magnetic interactions between particles at the nanometer scale in magnetic liquids.

Introduction

Ferrofluids are colloidal suspensions of magnetic nanoparticles dispersed in a liquid carrier (water, oil, organic solvent).[1] Particles consist of a ferro/ferrimagnetic material with a typical diameter in the 5-25 nm range, each of them being regarded as a single domain magnetic dipole. Ferrofluids are dual by nature, which results in a "normal" liquid behaviour in the absence of a magnetic field, while application of a moderate field allows controlling the liquid flow and modifying its physical characteristics (such as optical properties and viscosity).[2] This

a. Institut de Minéralogie, de Physique des Matériaux et de Cosmochimie (IMPMC), Sorbonne Université, CNRS, MNHN, UMR7590, CNRS, 4 place Jussieu, 75052 Paris Cedex 05, France.

b. Synchrotron SOLEIL, L'Orme des Merisiers, Saint-Aubin – BP48, 91192 Gif-sur-Yvette, France.

c. Laboratoire de Physicochimie des Electrolytes et Nanosystèmes Interfaciaux (PHENIX), Sorbonne Université, CNRS, PHENIX, F-75005 Paris, France.

d. Inorganic Chemistry and Catalysis, Debye Institute for Nanomaterials Science, Utrecht University, Universiteitsweg 99, 3584 CG Utrecht, The Netherlands.

e. Institute of Nanoscience and Nanotechnology, NCSR "Demokritos", 153 10 Aghia Paraskevi, Attiki, Greece

f. AGH University of Science and Technology, Academic Centre for Materials and Nanotechnology, Al. Mickiewicza 30, 30-059 Krakow, Poland.

g. Université Grenoble Alpes, CNRS, Institut de Recherche pour le Développement, Irstea, Météo France, OSUG, FAME, 38000 Grenoble, France.

h. Université de Paris, Institut de physique du globe de Paris (IPGP), CNRS, F-75005 Paris, France.

* Amelie.Juhin@upmc.fr

has led already for fifty years – since their invention by NASA-,[3] to numerous applications in technology (actuators, pumps, purification devices),[4,5] nanomedicine (drug delivery, magnetic hyperthermia),[6,7] and fine art.[8] The magnetically driven modification of macroscopic properties finds its origin at the nanoscale in the strong magnetic dipole interactions occurring between particles.[9] Nanoparticles can even self-assemble spontaneously into chains and rings at zero applied field when the dipole-dipole energy exceeds thermal fluctuations.[10,11] For ferrofluids, the effect of the modification of the microstructure is very interesting, not only in relation with the magnetic properties (for example, to optimize the efficiency in biomedical applications), but also with the mechanical[12] and optical properties.[13] Several studies have underlined that macroscopic magnetic properties of ferrofluids can significantly be altered by the interparticle magnetic interactions occurring at the nanoscale,[14–18] hence the idea that a fine understanding and tailoring of this nanoscale structuration could allow for a more effective engineering of novel magnetic responsive ferrofluids.[19,13]

The influence of magnetic dipole interactions in particle assemblies was questioned by de Gennes and Pincus in 1970,[20] and followed by theoretical studies which first focused on single-phase, monodispersed ferrofluids.[21,22] On the experimental side, observation of particle organization in ferrofluid dispersions remained a challenge during three decades, until the team of A. P. Philipse and co-workers was able to observe chain-like and ring-like structures of magnetite nanoparticles in vitrified dispersions using Cryogenic Transmission Electron Microscopy (Cryo-TEM).[23,24] In parallel,

theoretical, computational and experimental works have addressed the arrangement of particles in dipolar structure formation and the interplay between microstructure and macroscopic optical and magnetic properties in bidisperse ferrofluids.[25–29,17] The question of size polydispersity, which is inherent to the ferrofluid synthesis, appears to be a crucial point. Most of the synthetized ferrofluids are indeed naturally polydisperse, hence the need to produce a realistic structural model of single-phase ferrofluids that would be able to explain experimental observations. A first approximation of "real ferrofluids", *i.e.* including the size distribution of the particles, was made with theoretical models of bidisperse ferrofluids containing large and small particles,[30,31] which can behave as a mixture of strong and weak magnetic particles with an appropriate choice of the material and the particle size. The influence of dipolar interactions and of complex particle arrangements in bidisperse particle assemblies extends beyond the case of ferrofluids, since similar repercussions can be found for magnetorheological fluids[32] or elastomers[33]. It is worth noticing that from the experimental point of view, tending towards a real bidisperse ferrofluid (where particle sizes are in the 5-20 nm size range) requires a very narrow size distribution for the small and the large nanoparticles. Besides, the synthesis routes can yield different magnetic properties for similar sizes and this renders the interpretation complicated.[34–36] Another strategy to explore the effect of magnetic dipole interactions is to use a mixture of two ferrofluids with highly different magnetizations (such as one ferrimagnet and one paramagnet, or a hard ferrimagnet and a soft ferrimagnet), in order to produce a magnetically bidisperse system. For size bidisperse ferrofluids, where the difference in particle size of the two populations is not extremely large (usually the difference is between one and a couple of tens nanometers), the difference in magnetic anisotropy between both populations is indeed *(i)* partially blurred by size distribution, *(ii)* highly dependent on the temperature (*i.e.* above or below the blocking temperature for the individual nanoparticles). It can be noticed that dipole-dipole interactions are tuned by the value of the saturation magnetizations and the nearest neighbor distances. These two ingredients act differently for the case of size bidisperse ferrofluids compared to magnetically bidisperse ferrofluids. The latter, known as binary ferrofluids, are therefore a textbook case to study interparticle interactions in ferrofluids. In addition, such mixtures pave the way for fabrication of complex materials relevant for novel magneto-optical applications.[37–39]

However, only very few binary ferrofluids have been studied so far experimentally. In $CoFe_2O_4 – NiFe_2O_4$ ferrofluids, Han *et al* found the striking feature that the maximum magnetization is not a monotonous function of the paramagnetic $NiFe_2O_4$ concentration.[40] A similar effect was observed in dilute binary ferrofluids of strong magnetic γ-Fe_2O_3 nanoparticles mixed with weak ferrimagnetic $ZnFe_2O_4$ nanoparticles.[41] Recently, bulk magnetometry measurements were performed on solid state (dried) mixtures of γ-Fe_2O_3 and Co-doped γ-Fe_2O_3 nanoparticles and fitted by an empirical model, revealing that soft particles can soften the hard ones, while hard particles can harden the soft ones.[42] Nevertheless, whether the same conclusion holds

for ferrofluid samples remains an open question. The very few experimental investigations of binary ferrofluids performed so far have only provided limited or indirect information, because *(i)* bulk magnetometry measurements provide an average picture of the magnetic properties, *(ii)* TEM images measured on dried ferrofluids give evidence on the particle morphology, but not on the true particle distribution in the liquid phase. In addition, cryo-TEM investigation of binary ferrofluids with small particle size is rather challenging: first, because nanoparticles with spherical shape, small size, and low size polydispersity are best obtained with surfactants on the surface in highly volatile, organic solvents,[43] which makes the sample preparation more difficult, and second, because chemical analysis using energy dispersive X-ray spectroscopy (EDX) must be performed to disentangle both types of particles. All in all, little is known on the magnetic dipole interactions occurring in binary ferrofluids, whose structuration has never been investigated, and the role of each component in the collective magnetic properties has been only indirectly evidenced, by extrapolating a series of ferrofluids with different volume fractions and/or using some theoretical arguments. Consequently, although binary ferrofluids offer an unprecedented interplay of dipole interactions, potential applications related to their texturing are currently largely under explored.

Here we carry out an experimental study of a 1:1 binary ferrofluid consisting in two types of ferrimagnetic nanoparticles with 6 nm size, spherical shape and small size polydispersity, which have been synthesized following the high temperature decomposition of metal acetylacetonate process ("acac" process) and dispersed in heptane: $CoFe_2O_4$ nanoparticles that are "hard" ferrimagnetic particles and $MnFe_2O_4$ that are "soft" ferrimagnetic ones. The magnetic barrier energies of both types of nanoparticles are very different (the ratio of their coercive fields is on the order of 100) and we have studied the effect of their mutual interactions upon their respective magnetic properties. The kick-off observation motivating this study is that at low temperature, the bulk magnetization curve of a 0.2% vol. $CoFe_2O_4 – MnFe_2O_4$ binary (0.2% is the volume fraction of the total number of $CoFe_2O_4$ and $MnFe_2O_4$ nanoparticles) exhibits a wasp-waisted shape typical of two magnetic phases, but this magnetization curve does not superimpose with the linear combination of those measured for both single phase ferrofluids ($CoFe_2O_4$, $MnFe_2O_4$) (Supporting Information Figure S1). This suggests the existence of peculiar magnetic interactions occurring in the binary mixture despite the very low particle concentration, which prompted further investigations. The magnetic signature of each magnetic component was measured using an element selective experimental approach based on a core level magnetic spectroscopy, RIXS-MCD (X-ray Magnetic Circular Dichroism in Resonant Inelastic X-ray Scattering) that is performed at synchrotron radiation facilities. Comparison to the magnetic properties of the parent ferrofluids allowed to quantify the mutual influence of the $CoFe_2O_4$ and $MnFe_2O_4$ components, which was further confirmed by First Order Reversal Curves (FORC) measurements. Monte-Carlo simulations of collective magnetic properties were conducted, using the nanoscale particle organization measured by cryo-

TEM experiments. Our results show that even at such a low particle concentration, $MnFe_2O_4$ and $CoFe_2O_4$ nanoparticles interact through long-distance magnetic dipole interactions within small particle clusters, which results at the microscale in the modification of their respective magnetic coercivity. While the $CoFe_2O_4$ population act as "good neighbours" increasing the magnetic coercivity of the $MnFe_2O_4$ component, the latter behaves as a "bad neighbour" resulting in the reduction of the magnetic coercivity for the $CoFe_2O_4$ component.

Materials and Methods

Synthesis. Ferrofluids of nanoparticles with controlled morphology and excellent crystallinity were obtained using the thermal decomposition process of metallic acetylacetonate precursors in the presence of oleic acid, 1,2-hexadecanediol, oleylamine and benzyl ether, following the process of Sun *et al*.[43] The synthesis of $MnFe_2O_4$ and $CoFe_2O_4$ nanoparticles has been described elsewhere.[44]

Transmission Electron Microscopy. TEM micrographs were obtained using a JEOL 100 CX2. Size histograms were obtained from the analysis of the TEM micrographs over more than 10000 nanoparticles. These histograms were fitted by a lognormal law with a least-square refinement that provides particles mean diameter d_0 and their respective polydispersity σ.

Cryogenic Transmission Electron Microscopy. 3 µl of binary ferrofluid sample was drop-casted on the Quantifoil R2/1 TEM grid and plunge-frozen in liquid N2 using a Vitrobot (ThermoFischer). The grid was transferred under liquid N_2 to cryo-TEM holder, and 2k x 2k px STEM images were collected using a Talos^{TM} F200X (ThermoFischer) microscope operating at 200 kV. Elemental EDS maps were acquired using the same microscope equipped with Super-X G2 EDS detector and Velox^{TM} analytical and imaging software, at 200 kV with 2,4 Mx magnification. About 300 frames of 512 x 512 px with dwell time of 5 µs were recorded per EDS map, amounting to 6-7 min of acquisition time per map.

X-Ray Diffraction. XRD $\theta/2\theta$ patterns were recorded with a PANALYTICAL X'Pert Pro MPD diffractometer using Fe filtered the Co $K\alpha_1$ (λ = 1.79 Å) radiation from a mobile anode at 40 kV, 40 mA. The measurements were carried out in a range of 30°–80° 2θ in steps of 0.02° and collection time of 7200 s. Coherent domain sizes are calculated from the Scherrer equation.

Bulk Magnetic Measurements. Measurements were performed using a Vibrating Sample Magnetomer Quantum Design PPMS. Blocking temperatures were estimated from the Zero Field Cooled (ZFC) and Field Cooled (FC) temperature dependence of magnetization measured under a 70 Oe field on the particles dispersed in paraffin. Paraffin was used here to avoid the critical fusion point of heptane. Magnetization curve versus field measurements were performed at 25 K on the ferrofluids of the $MnFe_2O_4$, $CoFe_2O_4$, and $MnFe_2O_4$-$CoFe_2O_4$ particles.

RIXS and RIXS-MCD Spectroscopies. Experiments were carried out at ID26 beamline of the European Synchrotron Radiation Facility (Grenoble, France). Measurements were performed at the Co and Mn K-edges at low temperature on the frozen phase of ferrofluids using a dedicated liquid cell. The uncertainty on temperature was estimated to be +/- 5 K. The incident energy was selected using a pair of Si(311) crystals. The intensity of Mn and Co $K\alpha$ emission lines (of the inelastically scattered beam) was analysed using a set of four spherically bent Ge(111) and Si (531) crystals, respectively, arranged with an Avalanche Photo Diode in the Rowland Geometry with a scattering angle of 90°. The overall resolution was measured at 0.7 and 0.8 eV for Mn and Co, respectively. For both Co and Mn edges, *1s2p* RIXS planes were recorded as a set of Constant Energy Transfer scans over the energy of the $K\alpha_1$ line and of the K pre-edge. Additionally, absorption spectra were measured using high energy resolution fluorescence detection (HERFD) by setting the emission energy to the maximum of the $K\alpha$ line (6.9313 keV for Co, 5.8998 keV for Mn), namely HERFD-XAS. HERFD-MCD and RIXS-MCD experiments were carried out with the same setup as for HERFD-XAS and RIXS measurements, the differences being that *(i)* the incident beam is circularly polarized (instead of linearly polarized in the case of HERFD/RIXS), *(ii)* samples are kept in magnetic saturation using an electromagnet allowing to reach a magnetic field of 1.5 T, for which a detailed calibration curve was measured. The circular polarization was obtained using a 500 µm thick diamond (111) quarter wave plate set downstream the Si(311) monochromator, with a circular polarization degree estimated to be 75%. RIXS-MCD planes were recorded by reversing the photon helicity at each incident energy. RIXS-MCD and HERFD-MCD spectra were recorded in the region of the Co and Mn K pre-edge, after freezing the samples with no external magnetic field. The spectra were normalized such that the maximum of the polarization-averaged absorption spectrum is equal to 1 in the pre-edge region. Since *(i)* self-absorption corrections were found to be weak in the pre-edge range, *(ii)* all samples were measured in the same conditions and *(iii)* all MCD spectra are normalized to the pre-edge maximum, we assume that self-absorption effects do not impact our analysis.

Development of a liquid cell dedicated to RIXS-MCD measurements in liquid and frozen ferrofluids. The cryo-liquid cell setup for RIXS-MCD was designed in collaboration with the sample environment group of the ESRF. The setup is custom made and optimized to be compatible with the experimental chamber volume, high magnetic field, and ferrofluid materials. The sample holder is made of copper. A square cavity to receive the liquid sample is machined to suit the 90° scattering geometry used in the experiment. It is sealed by a 50 µm thick Kapton layer. The liquid cell is filled by injecting ferrofluids with a syringe through a side hole, which is later closed by a Vuiton O-ring and a screw. The sample holder is screwed to a cold plate cooled with a mini-cryostat using the principle of continuous flow helium circuit. The mini-cryostat consists of one heat exchanger. The main exchanger (the cold plate) cools the sample holder and a thermal shield protects the main exchanger and the sample itself from thermal radiation from the surrounding. A Kapton-sealed window is open in the thermal shield so that the beam reaches the sample. The setup allows a good vacuum with a pressure of 10^{-7} mbar and the temperature is set by monitoring the helium flow rate of the

mini-cryostat. The control of temperature is made by two thermometers, one located in the main exchanger and the other near the sample. Temperature can be regulated from 10 K to 300 K. However, in order to ensure the setting temperature as the effective temperature of the sample, we chose to work above 25 K.

Monte Carlo simulations of $MnFe_2O_4$, $CoFe_2O_4$ and binary mixture of $MnFe_2O_4$-$CoFe_2O_4$ ferrofluids. In our mesoscopic model, ferrimagnetic spherical nanoparticles are located at the sites of a cubic lattice of dimensions 20α x 20α x 20α where α is the lattice constant. Random distribution was considered for the single Co ferrite and the Mn ferrite nanoparticles samples with concentration c=0.2%. For the binary sample, clusters of nanoparticles were produced by dividing the box into eight areas of size 10α x 10α x 10α. Each nanoparticle cluster has different concentration (*i.e.* it consists of different number of nanoparticles (2 to 6) at random distances) (see Figure 3a) to describe the ferrofluid inhomogeneity but the mean particle concentration for the whole system is c=0.2%. In the case of the binary mixture, in one of the 8 clusters, the nanoparticles type and their positions were taken from the TEM micrograph.

Each nanoparticle is described by one "macro" spin vector for the core region $\vec{s}_{1i}$ and two others for the surface region ($\vec{s}_{2i}$ and $\vec{s}_{3i}$ where $1 \leq i \leq N$, with N the total number of particles). The magnetic moment for each spin is $m_n = M_n V_n / M_s V$. Here, V_n and M_n are the volume and the saturation magnetization of the core (n=1), the "up" (n=2) and the "down" (n=3) surface sublattices spins, V is the particle volume and M_S its saturation magnetization. Each spin has a uniaxial easy anisotropy axis randomly oriented.

The total energy of the system for the N nanoparticles is:[45]

$$E = -\frac{1}{2}\sum_{i=1}^{N}\left[J_{c1}\left(\vec{s}_{1i}\cdot\vec{s}_{2i}\right) + J_{c2}\left(\vec{s}_{1i}\cdot\vec{s}_{3i}\right) + J_{srf}\left(\vec{s}_{2i}\cdot\vec{s}_{3i}\right)\right] - \sum_{i=1}^{N}K_{srf}\left[V_2\left(\vec{s}_{2i}\cdot\hat{e}_{2i}\right)^2 + V_3\left(\vec{s}_{3i}\cdot\hat{e}_{3i}\right)^2\right]$$

$$-\sum_{i=1}^{N}K_c V_1\left(\vec{s}_{1i}\cdot\hat{e}_{1i}\right)^2 - \frac{1}{2}g\sum_{i,j=1,i\neq j,}^{N}\left(\sum_{n=1}^{3}m_{ni}\cdot\vec{s}_{ni}\right)\frac{3\hat{r}_{ij}\cdot\hat{r}_{ij}-1}{r_{ij}^3}\left(\sum_{n=1}^{3}m_{nj}\cdot\vec{s}_{nj}\right) - \sum_{i=1}^{N}\sum_{n=1}^{3}\mu_0 Hm_{ni}\left(\vec{s}_{ni}\cdot\hat{e}_h\right)$$

(Equation 1). The first energy term gives the intraparticle nearest neighbour exchange interactions for each nanoparticle. Inside the angular brackets the first and second term give the exchange interactions between the core spin and the two surface spins (with J_{c1} and J_{c2}, the intra-particle exchange coupling constants), and the third term the exchange interaction between the surface spins (with J_{srf} the surface exchange coupling). The second and third energy terms give the anisotropy energy for the surface (K_{srf}) and the core (K_c) respectively ($\hat{e}_{1i}$, $\hat{e}_{2i}$, $\hat{e}_{3i}$ being the anisotropy easy-axes direction). The fourth term gives the magnetostatic energy with the dipolar interactions among all spins in the nanoparticles, with $r_{ij} = |\vec{r}_i - \vec{r}_j|$ the distance between a pair of particles and $\hat{r}_{ij} = \vec{r}_{ij} / r_{ij}$ the corresponding unit vector. The last term is the Zeeman energy ($\hat{e}_h$ being the direction of the magnetic field).

To calculate the parameters entering Eq. (1) we have started from their bulk values and then rescaled them taking into account the number of atomic spins in the two sublattices, by employing an atomic scale modelling for the spinel structure of a 6 nm diameter particle.[41] These values become:

(a) j_{c1}= -4.5, j_{c2}= 2.0, j_{srf}= -2.35 (exchange coupling constants for both types of nanoparticles);

(b) k_C= 11 and k_{srf} =25 (effective anisotropy constants for $MnFe_2O_4$), and k_C= 100 and k_{srf} =230 (effective anisotropy constants for $CoFe_2O_4$) at 5 K. At higher temperatures, taking into account the anisotropy temperature dependence of Co ferrite nanoparticles[46] and Mn ferrite nanoparticles,[47] we have used a double Boltzmann function (Eq. (2), which describes the reduction of the effective anisotropy with temperature, for the core and the surface, in both types of nanoparticles:

$$k\left(T\right) = k(T=5\ K)\times[0.047 + 0.95\times(\frac{b}{1+e^{T-c}} + \frac{1-b}{1+e^{\frac{T-e}{f}}})] \qquad (Equation\ 2)$$

The parameters calculated from the temperature dependence of the experimental values of the coercivity and the ZFC magnetization of our samples and entering Eq. (2) are: c=27, e=200, *f* =70 and b=0.7 (for the core) b=0.8 (for the surface) for $MnFe_2O_4$ nanoparticles and c=30, e=300, *f*=30 and b=0.3 (for the core) b=0.4 (for the surface) for $CoFe_2O_4$ nanoparticles;

(c) assuming surface thickness of 0.85 nm, the magnetic moments of the three macrospins for the $MnFe_2O_4$ nanoparticles are: m_1=0.37, m_2=0.37, m_3=0.74 for $MnFe_2O_4$. From the experimental hysteresis loops $Ms_{CoFe2O4}$ = 1.45 $Ms_{MnFe2O4}$, therefore m_1=0.54, m_2=0.65, m_3=0.96 for $CoFe_2O_4$; (d) g ~ ((M_s^2 d^3) is the dipolar strength, where *d* is the size of the nanoparticles, consequently, *d* is the smallest interparticle distance. The dipolar strength is $g_{MnFe2O4}$=0.24, $g_{CoFe2O4}$=0.76 and $g_{MnFe2O4-CoFe2O4}$=0.52. The above energy parameters have been normalized by the factor $2k_BT$ (with T= 5 K), so they are dimensionless. The magnetic configuration was obtained by a Monte Carlo simulation, using the standard Metropolis algorithm.[48] Results obtained for a given temperature and applied field were averaged over 60 samples with various spin configurations, realizations of the easy-axes distribution and different spatial configurations for the nanoparticles following the standard hysteresis and ZFC-FC protocols.[41]

FORC diagrams. FORC diagrams were measured at 10 K with a magnetometer (μ-VSM) from Princeton Measurements Corporation at the IPGP-IMPMC Mineral Magnetism Analytical Facility. Ferrofluids were put in polycarbonate gelatine capsules traditionally used for liquids. Between 80 and 100 individual FORCs were measured to calculate each FORC diagram. These were analysed using the FORCinel software,[49] with a variable smoothing factor,[50] which considerably reduces the noise levels by applying larger smoothing factors to the background, while preserving the areas along the axes with relatively small smoothing factors. The smoothing parameters were the same for all the FORC diagrams analysed, in order to avoid introducing bias due to different smoothing for all the FORC diagrams analysed, in order to avoid introducing a bias due to different smoothing.
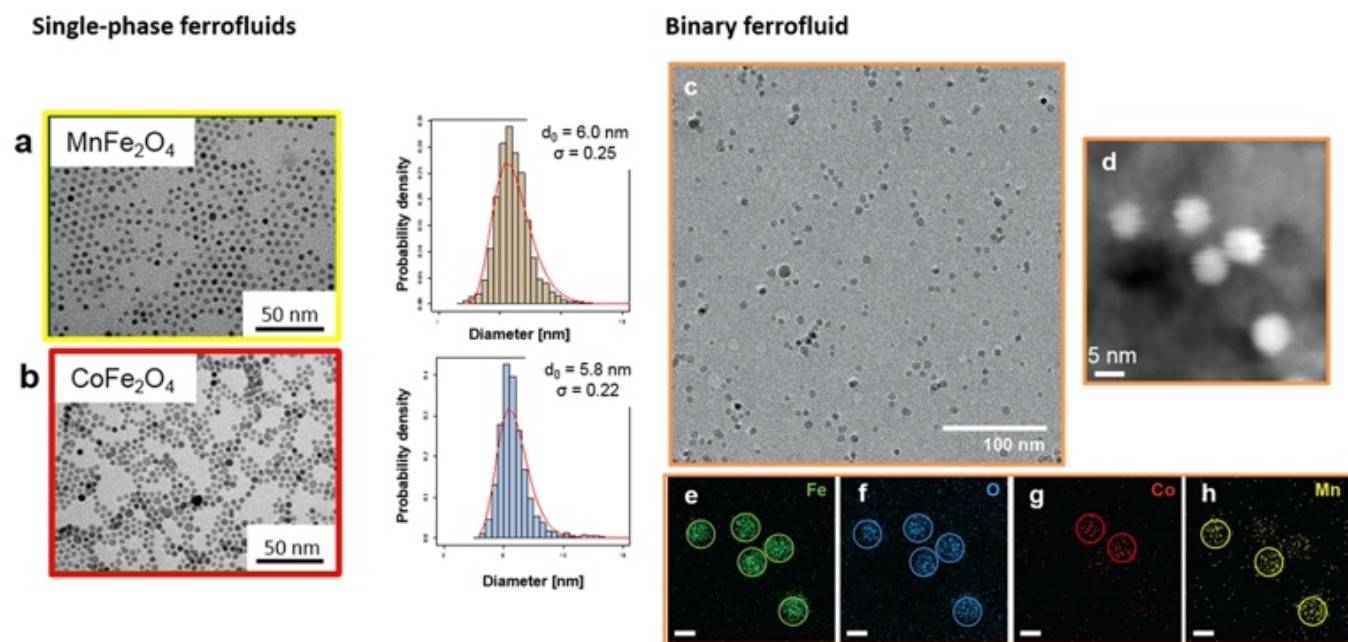
Single-phase ferrofluids

Binary ferrofluid

Figure 1- **Left panel:** Structural characterization of the pure MnFe$_2$O$_4$ (a) and CoFe$_2$O$_4$ (b) dried nanoparticles from the single-type particle ferrofluids: Transmission Electron Microscopy (TEM) images and associated particle size distribution histograms fitted by a log-normal distribution. **Right panel:** Cryo-TEM images of the CoFe$_2$O$_4$ − MnFe$_2$O$_4$ binary ferrofluid: Large scale, low magnification bright field TEM image showing the long range particle dispersion (c), High magnification high-angle annular dark field scanning TEM (HAADF-STEM) image (d) of a five particle assembly and EDX elemental map showing the distribution of Fe, O, Co and Mn (e, f, g, h) in the five particles shown in (d).

Results and discussion

In Figure 1 are shown the faceted nanoparticles of CoFe$_2$O$_4$ and MnFe$_2$O$_4$ dispersed as ferrofluids in heptane. Nanoparticles have a cubic spinel *Fd-3m* crystal structure (Supporting Information Figure S2*)*, a similar particle size of 6 nm and a narrow lognormal size distribution (with σ = 0.25 for the CoFe$_2$O$_4$ ferrofluid and σ = 0.22 for the MnFe$_2$O$_4$ ferrofluid). Typical hysteresis loops of magnetically hard CoFe$_2$O$_4$ and magnetically soft MnFe$_2$O$_4$ nanoparticles are obtained for the single-phase ferrofluids at 25 K (Supporting Information Figures S1 and S3). The CoFe$_2$O$_4$ − MnFe$_2$O$_4$ binary ferrofluid is obtained by mixing equal volumes of the parent ferrofluids with a particle volume fraction equal to 0.2 %: this value is much less than the threshold of 1% below which static magnetic interactions are usually considered negligible.[51,52] The images obtained by cryo–TEM measurements on the vitrified binary ferrofluid display, on the long range, well-distributed particles (Figure 1c).
Nevertheless, high magnification images reveal the formation of small clusters involving several nanoparticles (Figure 1d). EDX analysis indicates that these clusters contain both CoFe$_2$O$_4$ and MnFe$_2$O$_4$ particles, as can be seen from EDX elemental maps showing either strong Co or Mn signal (Figure 1e, f, g). In this particle assembly, in particular, the two smallest interparticle distances (centre to centre, measured as 6.3 nm and 8.7 nm) involve one CoFe$_2$O$_4$ and one MnFe$_2$O$_4$ particle: as the magnetic dipolar interaction decreases as *1/r³* where *r* is the interparticle distance, the existence of neighbouring CoFe$_2$O$_4$ and MnFe$_2$O$_4$ particles suggests the existence of long-range magnetic dipole

interactions involving both types of particles, which may be reflected in the macroscopic magnetic properties as discussed in the following.
The electronic and magnetic properties of the MnFe$_2$O$_4$ and CoFe$_2$O$_4$ components within the binary were probed separately by using the chemical selectivity of RIXS and RIXS-MCD spectroscopies performed at the Mn and Co *K*-edges, respectively, and a dedicated set-up developed for magnetic liquid samples (Figure 2a-c). Analysis of RIXS and RIXS-MCD spectra provides insights into the electronic and magnetic properties of the absorbing atom, respectively, which are indicative of its cationic repartition in the crystal structure and of the magnetic anisotropy.[53,54] The spectra measured at low temperature in both reference ferrofluids show spectral features similar in shape and intensity to spectra previously published on known spinel ferrites: Mn ions are all Mn^{2+} ions and predominantly located in the spinel tetrahedral sites, while Co ions are all high spin Co^{2+} ions occupying the octahedral sites of the spinel structure. The RIXS and RIXS-MCD signatures measured in the binary ferrofluid at low temperature (Figure 2d-e) are very similar to those measured in the single phase ferrofluids (Supporting Information Figures S4 and S5), which indicates that mixing MnFe$_2$O$_4$ and CoFe$_2$O$_4$ nanoparticles has not induced any major structural change of the individual components, therefore excluding diffusion of Mn ions into the CoFe$_2$O$_4$ nanoparticles or diffusion of Co ions into the MnFe$_2$O$_4$ nanoparticles.
Element selective magnetization curves were then measured in the frozen phase of the single-MnFe$_2$O$_4$, single-CoFe$_2$O$_4$ and binary CoFe$_2$O$_4$ − MnFe$_2$O$_4$ ferrofluids (Figure 2f,
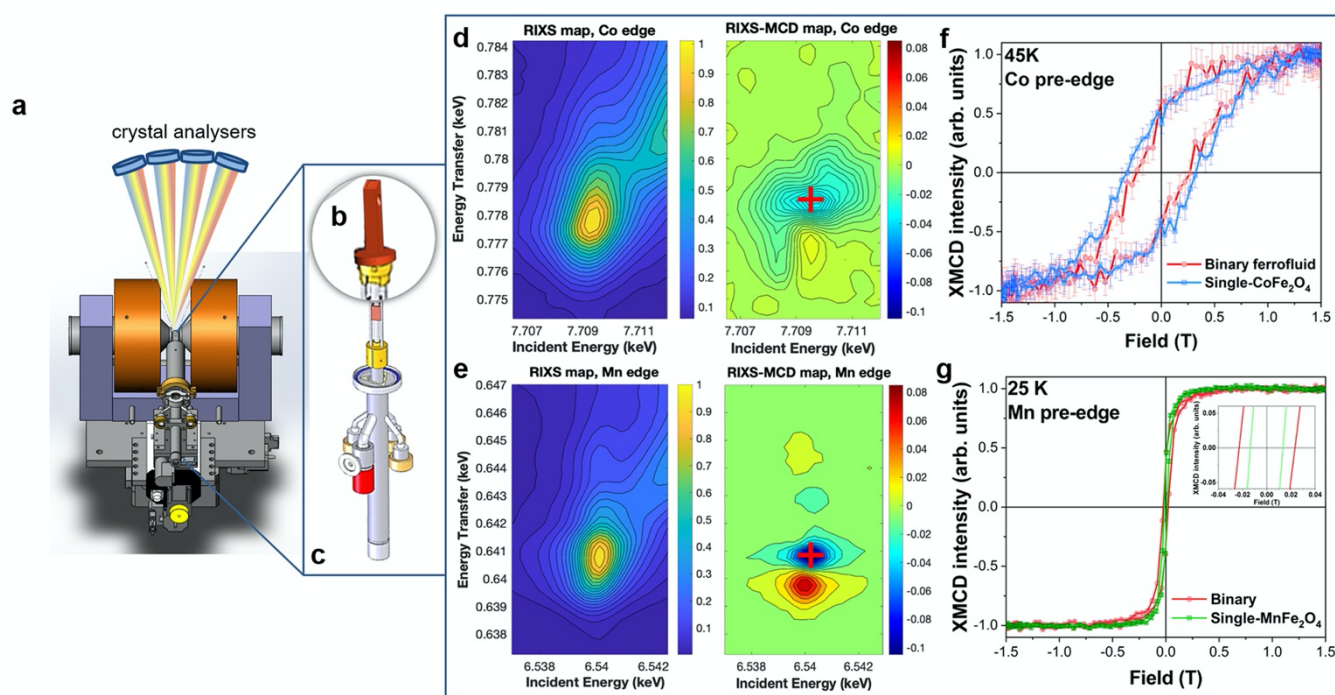
Figure 2- Left panel: Experimental setup developed for selective probing of the magnetization of $CoFe_2O_4$ and $MnFe_2O_4$ particles in ferrofluids (a), *i.e.*, a cryo-liquid cell (b) inserted in a cryostat (c) and adapted to the scattering geometry and the electromagnet. Magnetic couplings revealed by RIXS-MCD detected element specific magnetic curves: **Middle panel**: RIXS and RIXS-MCD spectra measured (d) at the Co edge (*T* = 45 K) and (e) at the Mn edge (*T* = 25 K) in the binary ferrofluid. **Right panel**: Element selective magnetization curves and error bars measured (f) at the Co edge in the frozen phase of $CoFe_2O_4$ (blue) and binary (red) ferrofluids, and (g) at the Mn edge in the frozen phase of $MnFe_2O_4$ (green) and the binary ferrofluids (red). The red cross on the RIXS-MCD spectra indicates the incident and emission energies used to measure the corresponding magnetization curve.

g), by fixing the incident and emission energies at the values that maximize the RIXS-MCD signal, first at the Co edge, then at the Mn edge. This allows disentangling in the binary ferrofluid the magnetic contributions stemming from either the $CoFe_2O_4$ nanoparticles or the $MnFe_2O_4$ nanoparticles, respectively. The external magnetic field was varied between -1.5 T and 1.5 T. At low temperature, the three ferrofluids present an opening of the magnetization curves. The coercive field measured at the Co *K*-edge at *T*=45 K in the binary ferrofluid is ~250 mT, which is 22 % lower than the one measured in the single-$CoFe_2O_4$ ferrofluid (~320 mT). The opposite trend is measured for the $MnFe_2O_4$ component, which shows a coercive field +77 % larger in the binary (~23 mT) than in the single-$MnFe_2O_4$ ferrofluid (13 mT). Although the values of coercivity measured at the Mn *K* -edge are rather small, we are confident that they are reliable because *(i)* the RIXS-MCD signal is large at the Mn edge and *(ii)* we took care to repeat the measurements several times to check for the consistency of our experimental findings as shown by the level of the error bars.

Having found evidence in the binary ferrofluid *(i)* of a non-additive behaviour of the bulk magnetization curve, *(ii)* of neighbouring $CoFe_2O_4$ and $MnFe_2O_4$ nanoparticles from cryo-TEM experiments and *(iii)* of modified magnetic properties for each component with respect to the parent samples from x-ray spectroscopies, we searched to establish a direct connection between these results. To that goal, Monte-Carlo simulations of magnetic properties (magnetization and susceptibility) were performed for both parent samples and for the $CoFe_2O_4$-

$MnFe_2O_4$ mixture. For the latter, we used a model particle distribution compatible with the cryo-TEM results, *i.e.* using particle positions extracted from Figure 1d. Each nanoparticle has a core/surface morphology described by a set of three classical "macro" spin vectors (one for the core, two for the surface layer) rendering the significant role of the surface contribution in the magnetic behaviour of such small particles.[45] In addition to inter-particle dipole interactions, short-range intra-particle exchange interactions (between the core spin with each of the two surface spins, and between the two surface spins in each particle) are accounted for. For $CoFe_2O_4$-$MnFe_2O_4$ mixture, we used a model particle distribution compatible with the cryo-TEM results, *i.e.* using particle positions extracted from Figure 1d. Indeed, we chose to use the true absolute particle volume fraction (0.2%) to model the clusters of particles, as depicted by the representative boxes of the different samples in Figure 3. Monte-Carlo simulations of the magnetization curves are shown in Figure 3 (left panel). In the binary ferrofluid, the coercive field of $CoFe_2O_4$ nanospinels is decreased by 9% with respect to the single phase ferrofluid, while the coercive field of the soft magnetic $MnFe_2O_4$ particles is increased by 94% with respect to the parent sample. This trend is in good agreement to the one measured by RIXS-MCD, although the calculation does not fully capture quantitatively the modification of magnetic properties, which we attribute to the fact that *(i)* in the experiment, the magnetic field accessible is only 1.5 T and there is an uncertainty on temperature of +/- 5 K, *(ii)* the ferrite atomic structure was not explicitly taken into
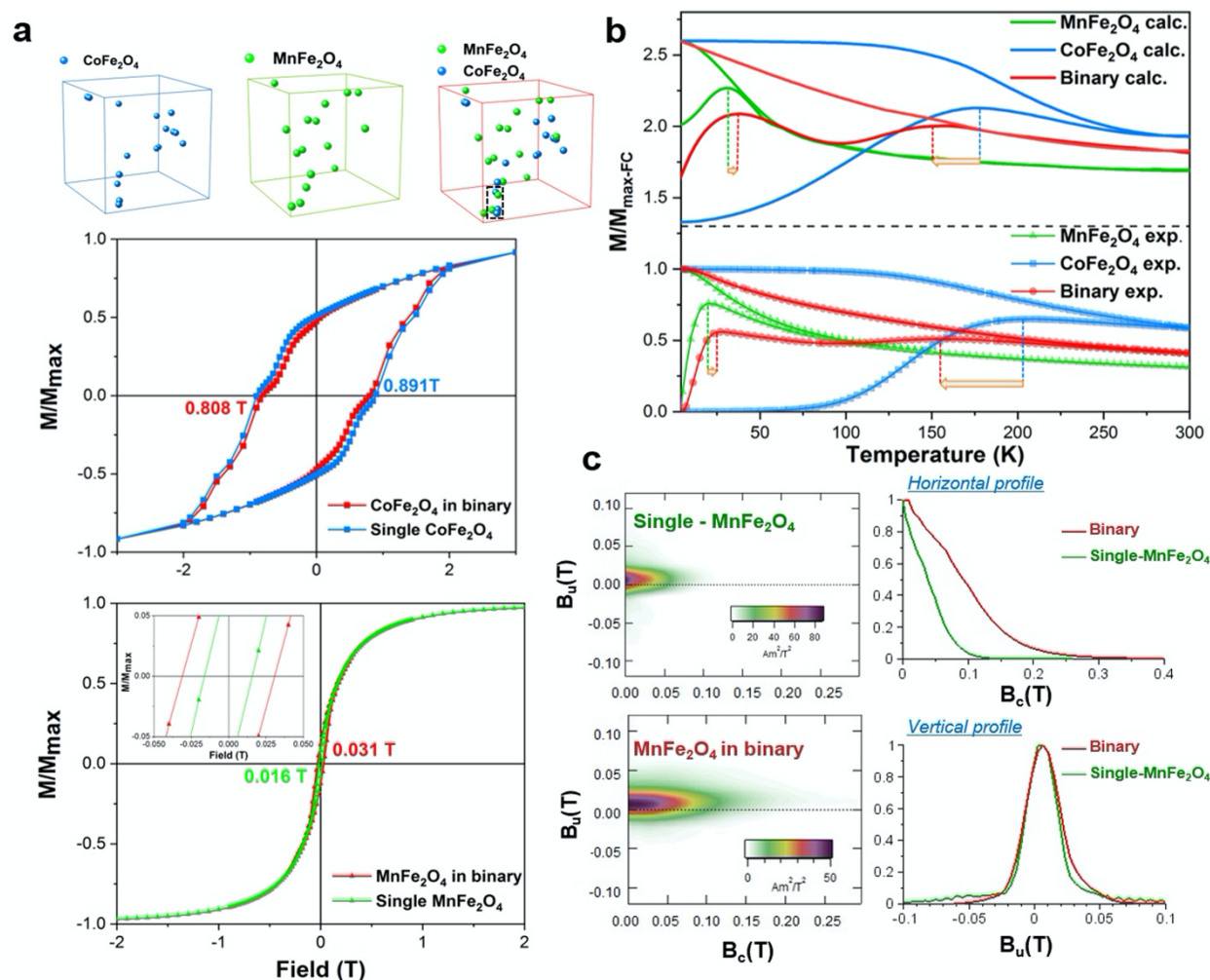
Figure 3- Left panel (a): Magnetization curves obtained by Monte Carlo simulations for CoFe$_2$O$_4$ (top, *T*=45 K) in the single-phase ferrofluid (blue squares) and the binary ferrofluid (red squares) and MnFe$_2$O$_4$ (bottom, *T*=25 K) in the single-phase ferrofluid (green circles) and the binary ferrofluid (red circles). **Top right panel (b)**: Field Cooled and Zero Field Cooled susceptibility curves obtained by Monte Carlo simulations (top, solid lines) and measured by bulk magnetometry (bottom, dotted lines) for the single-MnFe$_2$O$_4$ (green), single-CoFe$_2$O$_4$ (blue) and binary CoFe$_2$O$_4$ – MnFe$_2$O$_4$ (red) ferrofluids. **Bottom right panel (c)**: FORC diagrams measured at *T*=10 K (left) for MnFe$_2$O$_4$ and the binary zoom close to the origin where the peak due to MnFe$_2$O$_4$ is situated; normalized profiles (right) of these distributions through the maximum of the distributions.

account in the mesoscopic model used in our simulations. Nevertheless, simulations reveal that the modification of magnetic properties upon binary mixing finds its origin in the magnetic coupling occurring between neighbouring CoFe$_2$O$_4$ and MnFe$_2$O$_4$ nanoparticles in the mixture. These findings are also in line with the evolution of the zero-field-cooled (ZFC) and field-cooled (FC, using 7 mT induction) curves upon binary mixing (Figure 3 top right). In the experimental data, the blocking temperature, estimated at first approximation from the maximum of the ZFC curve, is reduced by 21% (from ~200 K to 157 K) for the CoFe$_2$O$_4$ component, while for MnFe$_2$O$_4$ ferrofluid, the blocking temperature is increased by 35% in the binary ferrofluid (from T$_B$ ~ 20 K to 27 K). The ZFC-FC curves simulated for the theoretical particle distribution of the three samples qualitatively show a similar evolution, thus supporting the idea that nanoscale magnetic dipole interactions occur in the binary due to short interparticle distances and result in the modification of macroscopic magnetic properties. First-Order Reversal Curve (FORC) diagrams (Figure 3 bottom right), obtained from multiple minor hysteresis curves, provide

additional information such as the distribution of microcoercivities (along the horizontal axis) and of interaction fields (along the vertical axis) of a sample.[55,56]

The horizontal profiles measured through the maximum of the peaks clearly show that the coercive field distribution of MnFe$_2$O$_4$ extends towards higher coercivities when MnFe$_2$O$_4$ is in the binary mixture, with respect to the single phase. This is consistent with the results of Monte-Carlo simulations (Figure 3 and Supporting Information Figure S6) and of x-ray magnetic spectroscopy measurements. Similarly, the vertical profiles of the FORC distributions show a very slight increase of the profile spreading when MnFe$_2$O$_4$ is in a binary ferrofluid: the full width at half maximum of the vertical profile is 27.7 mT for MnFe$_2$O$_4$ alone and 30.6 mT for MnFe$_2$O$_4$ in binary. Because the coercivity spectrum of CoFe$_2$O$_4$ extends well past the maximum field reached by the μ-VSM (approx. 1.5 T), we could not carry out a similar analysis on the CoFe$_2$O$_4$ component (Supporting Information Figure S7). The slight shift of the FORC features above the horizontal axis could be related to the "wishbone structure" widely obtained in measurements and numerical

ARTICLE   **Journal Name**

models of FORC diagrams for nanowire arrays,[57,58] which is asymmetric and also shifted above the horizontal axis.

Conclusions

In conclusion, we provided the nanoscale mechanism explaining the macroscopic magnetic properties of a physical mixture composed of soft and hard ferrimagnetic nanoparticles dispersed in heptane. Using a multi-scale combination of cryo-TEM/EDX, x-ray magnetic spectroscopy, bulk magnetometry, FORC measurements and Monte-Carlo simulations, we showed that despite the low particle volume fraction, the mixture does not behave as the average of individual components: the hard magnetic component becomes softer while the soft one becomes harder, which is due to nanoscale magnetic dipole interactions taking place between neighbouring soft and hard particles. This methodology can be extended to other multicomponent and/or self-organized magnetic fluids, whose more effective engineering requires a detailed understanding at the fundamental level. Our findings also open new perspectives to tailor novel magnetic responsive materials using magnetic dipole interactions between neighbouring nanoparticles with different magnetic properties.

Conflicts of interest

There are no conflicts to declare.

Author Contributions

Ph.S. and A.J. initiated and conceived the project. A.J. supervised the project. M.S, M.R., N.B, F.C., S.N., Ph. S., A.J., and N.D. performed the RIXS-MCD measurements. M.S., A.J., M.R. and Ph.S. provided the expertise on RIXS-MCD. M.S and A.J. analysed the RIXS-MCD measurements. M.S. implemented the code for the RIXS-MCD map analysis. M.R., A.J. and N.D. assisted to design the x-ray magnetic spectroscopy experiments and the liquid cell development. S.N. and V.G. synthesized the ferrofluids and realized the TEM imaging. V.D, V.G. and N.D. performed the magnetometry measurements. N.D. analysed the magnetometry measurements. N.D. performed the powder X-ray diffraction. J.Z., J.D.M., A.J. and N.D. assisted with the cryo-TEM experiments and J.V. performed the EDX measurements. D.T. provided the cryo-TEM analysis for the simulations. K.N.T and M.V. performed the Monte-Carlo simulations. C.C. and Y.G. performed and analysed the FORC measurements. N.D. and A.J. wrote the manuscript with the contribution from all co-authors. All authors have given the approval for the final version of the manuscript.

References

1   R. E. Rosensweig, *Ferrohydrodynamics*, Courier Corporation, 1997.
2   S. Odenbach, *J. Phys. Condens. Matter*, 2004, **16**, R1135–R1150.
3   S.S. Papell, US Pat., US3215572 A, 1965.
4   V. Bashtovoy and B. M. Berkovsky, *Ser. Learn. Mater. N. Y. Begell House*.
5   I. Torres-Díaz and C. Rinaldi, *Soft Matter*, 2014, **10**, 8584–8602.
6   D. K. Kim and J. Dobson, *J. Mater. Chem.*, 2009, **19**, 6294–6307.
7   B. Gleich and R. Weizenecker, *Nature*, 2005, **435**, 1214–1217.
8   S. Kodama, *Commun ACM*, 2008, **51**, 79–81.
9   L. M. Pop and S. Odenbach, *J. Phys. Condens. Matter*, 2006, **18**, S2785–S2802.
10 J. Li, J. Fu, Y. Lin, X. Liu, L. Lin and L. Chen, *AIP Adv.*, 2012, **2**, 042124.
11 J. Li, *Binary Ferrofluids and the Modulation Effect*, Sci Res Publ, Inc-Srp, Irvin, 2010.
12 P. Testa, R. W. Style, J. Cui, C. Donnelly, E. Borisova, P. M. Derlet, E. R. Dufresne and L. J. Heyderman, *Adv. Mater.*, 2019, **31**, 1900561.
13 Z. Di, X. Chen, S. Pu, X. Hu and Y. Xia, *Appl. Phys. Lett.*, 2006, **89**, 211106.
14 C. Martinez-Boubeta, K. Simeonidis, A. Makridis, M. Angelakeris, O. Iglesias, P. Guardia, A. Cabot, L. Yedra, S. Estradé, F. Peiró, Z. Saghi, P. A. Midgley, I. Conde-Leborán, D. Serantes and D. Baldomir, *Sci. Rep.*, **3**, 2013, 1652.
15 D. Faivre and M. Bennet, *Nature*, 2016, **535**, 235–236.
16 A. Pal, V. Malik, L. He, B. H. Erné, Y. Yin, W. K. Kegel and A. V. Petukhov, *Angew. Chem. Int. Ed.*, 2015, **54**, 1803–1807.
17 E. Siebert, V. Dupuis, S. Neveu and S. Odenbach, *J. Magn. Magn. Mater.*, 2015, **374**, 44–49.
18 D. Toulemon, M. V. Rastei, D. Schmool, J. S. Garitaonandia, L. Lezama, X. Cattoën, S. Bégin-Colin and B. P. Pichon, *Adv. Funct. Mater.*, 2016, **26**, 2454–2462.
19 X. Liu, N. Kent, A. Ceballos, R. Streubel, Y. Jiang, Y. Chai, P. Y. Kim, J. Forth, F. Hellman, S. Shi, D. Wang, B. A. Helms, P. D. Ashby, P. Fischer and T. P. Russell, *Science*, 2019, **365**, 264–267.
20 P. G. de Gennes and P. A. Pincus, *Phys. Kondens. Mater.*, 1970, **11**, 189–198.
21 W.-F. Ding, Z. Li, H. Zhou, B. Zhao, J. Wan, F. Song and G.-H. Wang, *J. Phys. Chem. C*, 2012, **116**, 10805–10813.

22 E. S. Minina, A. B. Muratova, J. J. Cerdá and S. S. Kantorovich, *J. Exp. Theor. Phys.*, 2013, **116**, 424–441.

23 K. Butter, P. H. H. Bomans, P. M. Frederik, G. J. Vroege and A. P. Philipse, *Nat. Mater.*, 2003, **2**, 88–91.

24 M. Klokkenburg, C. Vonk, E. M. Claesson, J. D. Meeldijk, B. H. Erné and A. P. Philipse, *J. Am. Chem. Soc.*, 2004, **126**, 16706–16707.

25 T. Kruse, A. Spanoudaki and R. Pelster, *Phys. Rev. B*, 2003, **68**, 054208.

26 T. Kristóf and I. Szalai, *Phys. Rev. E*, 2003, **68**, 041109.

27 A. O. Ivanov and S. S. Kantorovich, *Phys. Rev. E*, 2004, **70**, 021401.

28 M. Klokkenburg, R. P. A. Dullens, W. K. Kegel, B. H. Erné and A. P. Philipse, *Phys. Rev. Lett.*, 2006, **96**, 037203.

29 E. Pyanzina, S. Kantorovich, J. J. Cerdà and C. Holm, *J. Magn. Magn. Mater.*, 2011, **323**, 1263–1268.

30 A. Y. Zubarev and L. Y. Iskakova, *Phys. Stat. Mech. Its Appl.*, 2004, **335**, 314–324.

31 J. P. Huang, Z. W. Wang and C. Holm, *J. Magn. Magn. Mater.*, 2005, **289**, 234–237.

32 D. Susan-Resiga, D. Bica and L. Vékás, *J. Magn. Magn. Mater.*, 2010, **322**, 3166–3172.

33 P. A. Sánchez, O. V. Stolbov, S. S. Kantorovich and Y. L. Raikher, *Soft Matter*, 2019, **15**, 7145–7158.

34 N. Daffé, F. Choueikani, S. Neveu, M.-A. Arrio, A. Juhin, P. Ohresser, V. Dupuis and P. Sainctavit, *J. Magn. Magn. Mater.*, 2018, **460**, 243–252.

35 N. Daffé, V. Gavrilov, S. Neveu, F. Choueikani, M.-A. Arrio, A. Juhin, P. Ohresser, V. Dupuis and P. Sainctavit, *J. Magn. Magn. Mater.*, 2019, **477**, 226–231.

36 J. van Rijssel, B. W. M. Kuipers and B. H. Erné, *J. Magn. Magn. Mater.*, 2015, **380**, 325–329.

37 T.-Z. Zhang, J. Li, H. Miao, Q.-M. Zhang, J. Fu and B.-C. Wen, *Phys. Rev. E*, 2010, **82**, 021403.

38 J. Fu, J. Li, Y. Lin, X. Liu, H. Miao and L. Lin, *Sci. China Phys. Mech. Astron.*, 2012, **55**, 1404–1411.

39 J. Li, Y. Lin, X. Liu, B. Wen, T. Zhang, Q. Zhang and H. Miao, *Opt. Commun.*, 2010, **283**, 1182–1187.

40 S. Han, J. Li, R. Gao, T. Zhang and B. Wen, *Appl. Phys. A*, 2009, **98**, 179–186.

41 J. Fu, J. Li, Y. Lin, X. Liu, L. Lin and L. Chen, *Appl. Phys. A*, 2012, **108**, 155–160.

42 E. H. Sanchez, M. Vasilakaki, S. S. Lee, P. S. Normile, G. Muscas, M. Murgia, M. S. Andersson, G. Singh, R. Mathieu, P. Nordblad, P. C. Ricci, D. Peddis, K. N. Trohidou, J. Nogues and J. A. De Toro, *Chem. Mater.*, DOI:10.1021/acs.chemmater.9b03268.

43 S. Sun, H. Zeng, D. B. Robinson, S. Raoux, P. M. Rice, S. X. Wang and G. Li, *J. Am. Chem. Soc.*, 2004, **126**, 273–279.

44 V. Gavrilov-Isaac, S. Neveu, V. Dupuis, D. Taverna, A. Gloter and V. Cabuil, *Small*, 2015, **11**, 2614–2618.

45 M. Vasilakaki, G. Margaris, D. Peddis, R. Mathieu, N. Yaacoub, D. Fiorani and K. Trohidou, *Phys. Rev. B*, 2018, **97**, 094413.

46 Y. Zhang, Y. Liu, C. Fei, Z. Yang, Z. Lu, R. Xiong, D. Yin and J. Shi, *J. Appl. Phys.*, 2010, **108**, 084312.

47 S. Yoon, *J. Korean Phys. Soc.*, 2011, **59**, 3069–3073.

48 M. Vasilakaki, G. Margaris and K. Trohidou, in *Nanoparticles Featuring Electromagnetic Properties: From Science to Engineering*, Alessandro Chiolerio and Paolo Allia, 2012, p. 105.

49 R. J. Harrison and J. M. Feinberg, *Geochem. Geophys. Geosystems*, **9**, 2008, DOI:10.1029/2008GC001987.

50 R. Egli, *Glob. Planet. Change*, 2013, **110**, 302–320.

51 E. Dubois, V. Cabuil, F. Boué and R. Perzynski, *J. Chem. Phys.*, 1999, **111**, 7147–7160.

52 E. Dubois, Paris 6, 1997.

53 M. Sikora, A. Juhin, T.-C. Weng, P. Sainctavit, C. Detlefs, F. de Groot and P. Glatzel, *Phys. Rev. Lett.*, 2010, **105**, 037202.

54 A. Juhin, A. López-Ortega, M. Sikora, C. Carvallo, M. Estrader, S. Estradé, F. Peiró, M. D. Baró, P. Sainctavit, P. Glatzel and J. Nogués, *Nanoscale*, 2014, **6**, 11911–11920.

55 C. R. Pike, A. P. Roberts and K. L. Verosub, *J. Appl. Phys.*, 1999, **85**, 6660–6667.

56 A. Stancu, C. Pike, L. Stoleriu, P. Postolache and D. Cimpoesu, *J. Appl. Phys.*, 2003, **93**, 6620–6622.

57 C. R. Pike, C. A. Ross, R. T. Scalettar and G. Zimanyi, *Phys. Rev. B*, 2005, **71**, 134407.

58 C.-I. Dobrotă and A. Stancu, *Phys. B Condens. Matter*, 2015, **457**, 280–286.